Kefeng Li, Changjiang Song, Qijie Zhai, Mihai Stoica, Jürgen Eckert

Microstructure evolution of gas-atomized Fe–6.5 wt% Si droplets

Diese Version ist verfügbar / This version is available on:

https://nbn-resolving.org/urn:nbn:de:bsz:14-qucosa2-390478

SLUB
Wir führen Wissen.

TECHNISCHE UNIVERSITÄT DRESDEN

QUCOSA
Quality Content of Saxony

Microstructure evolution of gas-atomized Fe–6.5 wt% Si droplets

Kefeng Li
Department of Metallurgical Engineering, School of Materials Science and Engineering, Shanghai University, Shanghai 200072, People's Republic of China; and Institute for Complex Materials, Institute for Solid State and Materials Research Dresden, Dresden D-01069, Germany

Changjiang Song[a)] and Qijie Zhai
Department of Metallurgical Engineering, School of Materials Science and Engineering, Shanghai University, Shanghai 200072, People's Republic of China

Mihai Stoica
Institute for Complex Materials, Institute for Solid State and Materials Research Dresden, Dresden D-01069, Germany

Jürgen Eckert
Institute for Complex Materials, Institute for Solid State and Materials Research Dresden, Dresden D-01069, Germany; and Dresden University of Technology, Institute of Materials Science, Dresden D-01062, Germany

The magnetic Fe–6.5 wt% Si powder was produced by gas atomization and its microstructure was also investigated. The secondary dendritic arm spacing (SDAS) is related to the droplet size, $\lambda = 0.29 \cdot D^{0.5}$, and the numerical solidification model was applied to the system, giving rise to the correlation of microstructure to the solidification process of the droplet. It is found that the solid fraction at the end of recalescence is strongly dependent on the undercooling achieved before nucleation; the chances for the smaller droplets to form the grain-refined microstructures are less than the larger ones. Furthermore, the SDAS is strongly influenced by the cooling rate of post-recalescence solidification, and the relationship can be expressed as follows, $\lambda = 74.2 \cdot \left(\dot{T}\right)^{-0.347}$. Then, the growth of the SDAS is driven by the solute diffusion of the interdendritic liquids, leading to a coarsening phenomenon, shown in a cubic root law of local solidification time, $\lambda = 10.73 \cdot \left(t_f\right)^{0.296}$.

I. INTRODUCTION

The Fe–6.5 wt% Si magnetic material has excellent soft magnetic properties such as the highest magnetic permeability, minimum core loss,[1] and almost zero magnetostriction,[2] which make the material especially suitable for magnetic cores of inductive devices working at high frequency. However, the ductility of the steel is too poor to produce sheets by conventional rolling. The application of the material is therefore hindered. To overcome the poor workability of the alloy, preparation routes such as chemical vapor deposition (CVD)[3] and fast quenching ribbon[4] were used. But the vital drawbacks of these methods are their high cost and low production rate. Therefore, the spray forming process, a near net shape solution[5] and soft magnetic composite materials,[6] the combination of magnetic powders and insulators, are developed to provide materials with high permeability, excellent magnetic saturation, and high electrical resistivity.[7]

Both of the methods are based on the gas atomization process, which is commonly used to fabricate powders because of its low cost and mass production. The microstructures of gas-atomized powders are strongly related to their particle sizes, which in turn are believed to have an apparent effect on the magnetic performance.[8] The microstructure evolution is very important because it provides valuable information for the powder production, for example the secondary dendrite arm spacing (SDAS) is closely associated with particle size and cooling rates. The characterization of powder microstructure is of fundamental importance to optimize the atomization parameters, which are important to control the production process. Many research studies have been reported on various alloys, such as Cu–Sn[9,10] and Al–Si and Al–Cu,[11] Al–Fe,[12] super alloy,[13] and amorphous Al-based alloy.[14] On the other hand, the microstructure of the droplet is believed to be strongly affected by the undercooling before nucleation,[15] and this effect only becomes significant when the size of the droplet is around 10 μm or smaller.[12] Since it is impossible to measure the undercooling and nucleation of a flying droplet in atomizing chamber, numerical modeling is believed to be an effective approach to reveal thermalphysics of powder atomization, and numerous models have been developed,[16–25] in which the effects of atomization parameters on the solidification of the droplets were addressed. By combining the heat transfer analysis

---
[a)]Address all correspondence to this author.
   e-mail: riversxiao@163.com

with classic heterogeneous nucleation theory, the whole solidification process of the droplet is predictable. This work tends to conduct research on the microstructure characterization and thermal history calculation of the gas-atomized Fe–6.5% Si droplets. The results can be helpful to optimize the processing parameters of Fe–6.5 wt% Si magnetic powders.

II. EXPERIMENTAL DETAILS

Industry-grade pure iron (99.5%), silicon (99.9%), and nitrogen (99.9%) were used as starting materials and atomizing gas. The melting and atomization was done in a two-chamber vertical device. 10 kg Fe and Si raw materials were first induction melted in the upper chamber under 10^{-3} bar vacuum and kept for 10 min to reach homogeneity at ~1800 K (100 K above the liquidus), which is monitored by a Ray-tek infrared two-color pyrometer. The molten alloys were then poured into a crucible, preheated to the same temperature and goes down through the tip of the tube; the stream was disintegrated into droplets by the impact of high-pressure nitrogen gas from a close-coupled nozzle. Powders were then collected and sieved into eight size fractions for further analyses: <38, 38–53, 53–63, 63–75, 75–105, 105–150, 150–180, and >180 μm. Only powders below 180 μm were considered, because powders larger than 180 μm contained too many flakes or satellite particles.

The crystalline phases of the as-atomized powders were determined by x-ray diffraction (XRD) using monochromatic Cu K$_\alpha$ radiation produced by a Rigaku D/max-2550 diffractometer (Japan). The powders were first embedded in epoxy resin, in a 10 mm copper tube, and then the sample was mechanically polished and etched using 5% (volume fraction) natal. The observation of cross-sectional microstructures and surface morphology was carried out on an APOLO300 scanning electron microscope equipped with energy dispersive x-ray spectroscopy (EDX).

III. EXPERIMENTAL RESULTS

Figure 1 shows the particle size distribution of an atomization experiment, and the average particle diameter is $d_{50} = 127$ μm. In fact, the particle size distribution shows two local maxima: particles with 38–53 μm diameter and 75–106 μm diameter. The size distribution of the atomized powder particles depends on processing parameters such as gas pressure, melt overheating, heat capacity, and thermal conductivity of the atomizing gas, as well as the physical properties of the melting material. As it was mentioned in the experimental part, particles with diameters >180 μm were not further considered because of their irregular shapes.

From the Fe–Si phase diagram[26] in Fig. 2(a), the α-Fe (Si) solid solution phase is expected. The room temperature
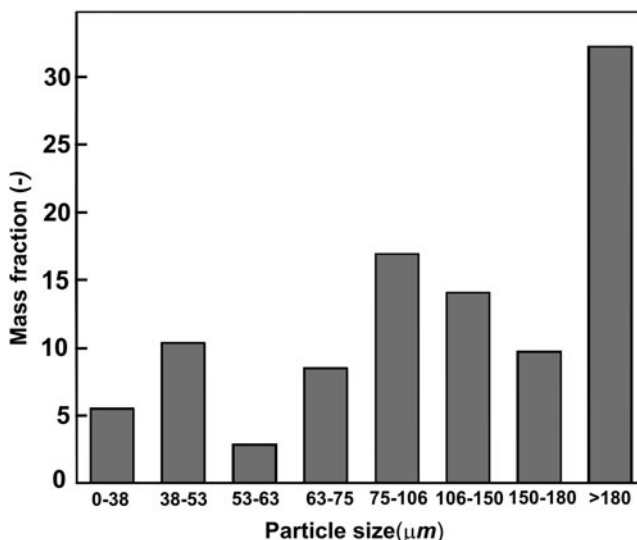

FIG. 1. Mass fraction of particles as a function of as-atomized Fe–6.5 wt% Si alloy powders.

XRD patterns of the as-atomized particles are shown in Fig. 2(b); a single phase α-Fe (Si) solid solution with no apparent differences indicating that phase formation is independent of solidification process. This result is consistent with what we can expect from phase diagram.

Direct observations of the as-atomized particles showed that the powders were mainly spherical in shape [Fig. 3(a)]. The size of the selected particles is about 140 μm [Fig. 3(b)], 60 μm [Fig. 3(c)], and 25 μm [Fig. 3(d)], respectively. Large and medium particles usually have many satellite particles attached during the solidification process in the turbulent gas flow. The morphology of the particles and their surfaces can be deduced from Figs. 3(b)–3(d). The dendritic, elongated dendritic, and equiaxed-type microstructures were observed. The micrometer-sized dendrite morphology indicates a relatively fast growth.[27]

The SDASs were measured using the cross-sectional image, as shown in Fig. 4. The dendrite patterns of the cross-sectional image as shown in Fig. 4(a) are not apparent because the distribution coefficient k in Fe–Si system is 0.8, very close to unity, causing less Si segregation as shown by the EDX results in Fig. 4(b). The EDX measurement was conducted in the encircled area of Fig. 4(a). The concentration of Si in white dots is higher than the surrounding interdendritic areas. The typical equiaxed dendrites and elongated dendrites of the Fe–Si alloy are indicated by Figs. 4(c) and 4(d).

IV. MODEL DESCRIPTION

To show the effect of atomization parameters on the microstructure, the droplet cooling model is briefly introduced here. The melt is firstly disintegrated into fine droplets by the impact of high-pressure inert gas
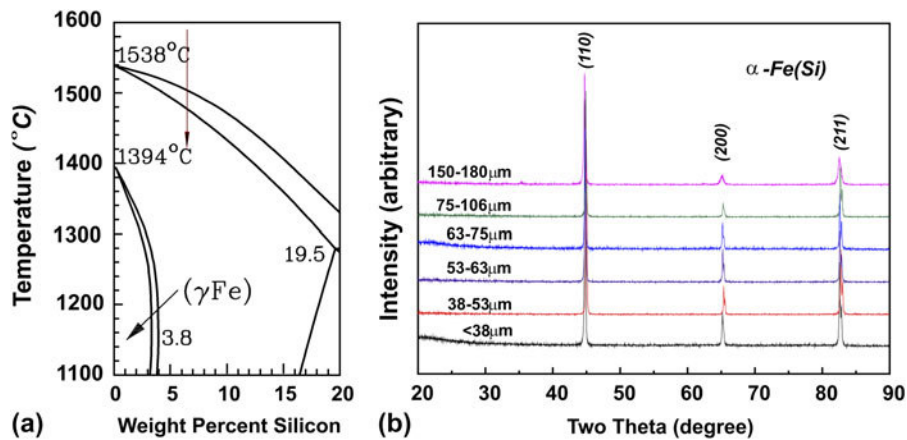
FIG. 2. (a) The Fe-rich part of Fe–Si phase diagram, where the red arrow shows the current composition, and (b) XRD patterns for as-atomized Fe–6.5 wt% Si atomized powders.
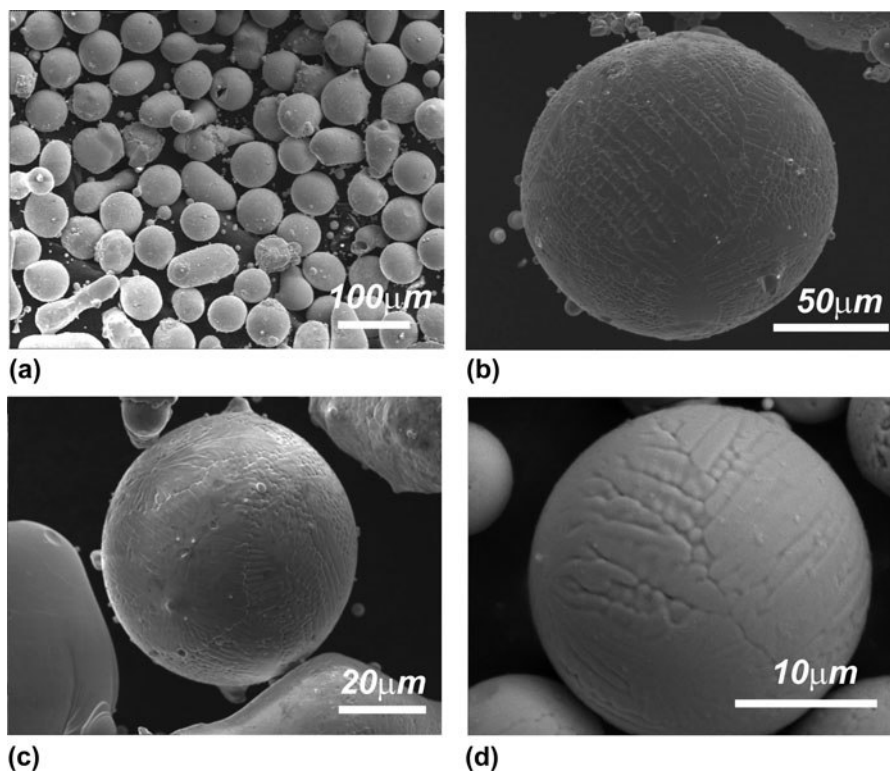

FIG. 3. Surface morphologies of atomized particles. (a) The overall spherical shape and the dendrite growth morphology of particles with diameters of (b) 140 μm, (c) 60 μm, and (d) 25 μm, are illustrated.

jets, and then droplets are accelerated and cooled down during flight in gas flow. By calculating the heat and momentum exchange of a droplet and gas, combined with classical nucleation theory, the cooling curve of a single droplet is traceable. The overall solidification of a droplet includes: cooling of liquids fully to its nucleation temperature, recalescence until the production of internal heat equals the heat transfer from the droplet surface, and segregated solidification to solidus temperature. First, the droplet cools down to its

nucleation temperature T_N. By safely neglecting the radiation effect, the heat exchange by convection is formulated as[20]

$$C_L \frac{dT_d}{dt} = -\frac{6h}{\rho_d D}(T_d - T_g) \quad , \tag{1}$$

where C_L, T_d, h, ρ_d, D, T_d, T_g are liquid specific heat, droplet temperature, heat transfer coefficient, density, diameter of the droplet, the droplet temperature, and
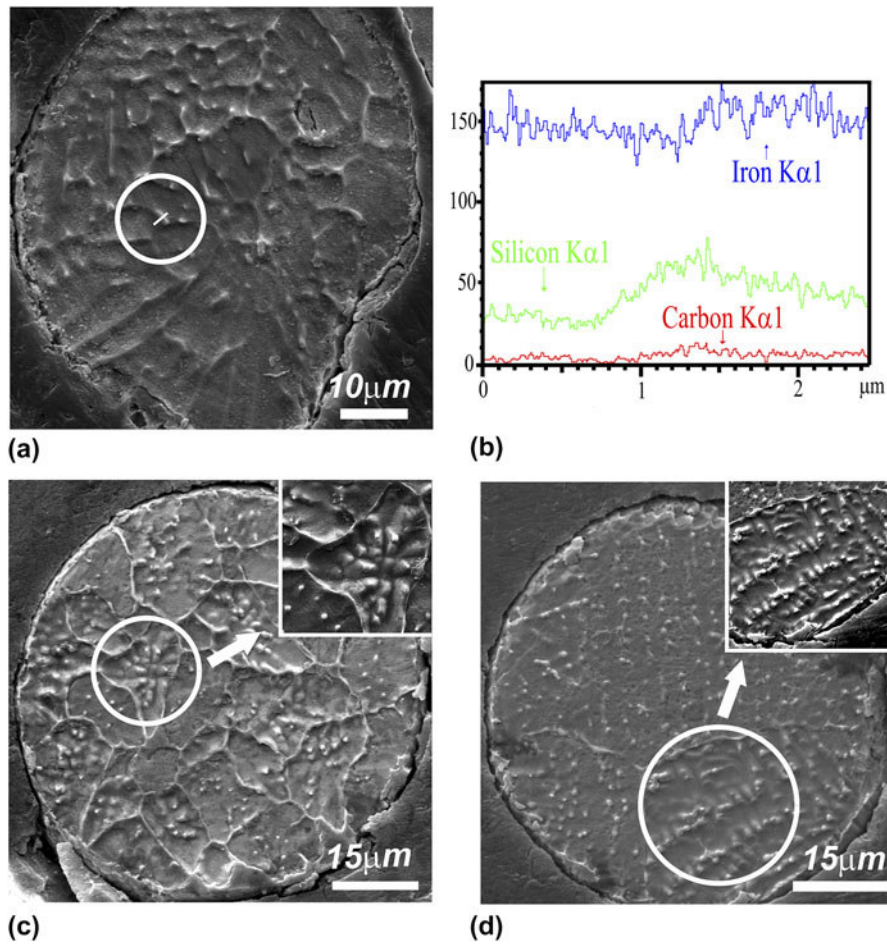
FIG. 4. (a) Cross-sectional images of Fe–Si particles and (b) EDX result of a line scan through an interdendritic area [encircled in Fig. 4(a)]. (c) Typical equiaxed dendritic and (d) elongated dendritic patterns are shown. Insets are the zoomed regions shown in (c) and (d).

temperature of the gas, respectively. At the end of this stage, T_d undercools to nucleation temperature,

$$T_N = T_L - \Delta T_{het} \quad , \tag{2}$$

where T_L is the temperature of liquid state droplet, and ΔT_{het}, the undercooling for heterogeneous nucleation can be expressed as[19]

$$\Delta T_{het} = \Delta T_{hom} \exp\left(-2.2 \times 10^{12} V_d\right) \quad , \tag{3}$$

According to the nucleation theory,[28] ΔT_{hom}, the undercooling for homogeneous nucleation can be evaluated as[24]

$$\Delta T_{hom}^2 = \frac{16\pi \sigma_m^3 \Omega_v^2 T_L^2}{3k_B(T_L - T_{hom})H_f^2 \ln\left(10^{44} V_d \frac{\Delta T_{hom}}{\dot{T}}\right)} \quad , \tag{4}$$

where σ_m, Ω_v, k_B, H_f, V_d, $\dot{T}$ are solid–liquid interface energy, atomic volume, Boltzmann constant, latent heat of fusion, volume of the droplet, and cooling rate, respectively.

Figures 5(a) and 5(b) illustrate examples of a single nucleation event within the droplet at the surface; the growth direction is shown by arrows. Figure 5(c) shows the preserved curvature of the solidification front from the surface, which is an imaginary envelope of primary dendrite stems.[16] During recalescence, the front moves at a very high speed, and the heat of fusion released heat up the droplet to its liquidus almost adiabatically within less than 10^{-5} S. Then, in the segregation growth stage, the dendrite network forms driven by heat extraction and the SDASs are determined by the cooling rate of the droplet.

The heat flow equation during recalescence for a solidifying droplet is given as below

$$C_{pd}\frac{dT_d}{dt} = \Delta H_d \frac{df_s}{dx} \cdot \frac{dx}{dt} - \frac{6h}{\rho_d}(T_d - T_g) \quad , \tag{5}$$

where $C_{pd} = (1 - f_s)C_L + C_S f_s$ and $\Delta H_d = \Delta H_f - (C_L - C_S)(T_L - T_d)$ are the integrated specific heat and latent heat of fusion, respectively. The quantities $\Delta H_f, f_s, T_d, \rho_d, D, h, T_g$ are latent heat per

530

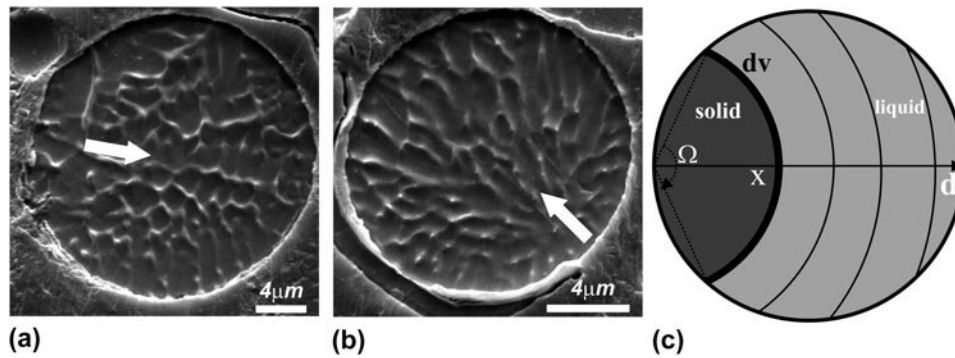J. Mater. Res., Vol. 29, No. 4, Feb 28, 2014

FIG. 5. Solidification processes with single nuclei at the surface of a droplet. (a) and (b) – Images of cross sections, arrows deduce the directions of solidification. (c) Schematic illustration of the solidification front.

unit mass, solid fraction, the instantaneous temperature, density, and diameter of the droplet, heat transfer coefficient, and gas temperature, respectively.

The moving rate of the solid phase along the axis in Fig. 5(c) can be formulated as[16]

$$\frac{dx}{dt} = K_i(T_L - T_d) \quad , \tag{6}$$

where K_i is the solid–liquid interface mobility. Also from Fig. 5(c), the volume fraction of the solidified cap can be calculated as

$$f_s = 4\left(\frac{x}{D}\right)^3 - 3\left(\frac{x}{D}\right)^4 \quad . \tag{7}$$

In this stage, the drastic release of heat of fusion heats up the droplet to the vicinity of its melting point. By setting $\frac{dT_d}{dt} = 0$, recalescence ends at the temperature T_r with the solid fraction f_r. Then, the segregated solidification continues, ruled by

$$C_{pd}\frac{dT_d}{dt} = \Delta H_d \frac{df_s}{T_d} \cdot \frac{dT_d}{dt} - \frac{6h}{\rho_d}(T_d - T_g) \quad , \tag{8}$$

where the solid fraction has a different expression with the recalescence stage

$$f_s = 1 - (1 - f_r)\left[\frac{T_M - T_r}{T_M - T_d}\right]^{1/1-k} \quad , \tag{9}$$

where T_M is the melting temperature of a pure solvent, here it refers to iron.

Then the solidification ends when T_d reaches its solidus temperature. The parameter set used for calculation is presented in Table I.

V. RESULTS DISCUSSION

From Eqs. (1)–(9), the undercooling and solid fraction as a function of the droplet size is obtained in Fig. 6 and Table II. It is apparently seen that as the droplet size

TABLE I. Thermo-physical properties of Fe–6.5 wt% Si alloy.[26,29,30]

Parameters	Unit	Value
C_L	J/kg/K	824.11
C_L	J/kg/K	761.96
ΔH_f	J/kg	2.47×10^5
σ_m	J/m^{-3}	204×10^{-3}
Ω_V	m^3/mol	7.1×10^{-6}
k	–	0.8
T_L	K	1706
T_M	K	1803

TABLE II. Calculated undercooling, the solid fraction, and temperature at the end of recalescence for droplets of different sizes.

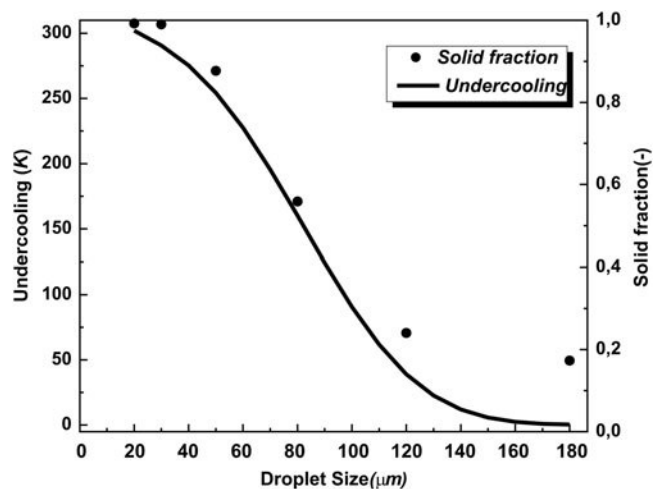| Droplet size (µm)	ΔT_{het} (K)	f_r (%)	T_r (K)
20	302	99.2	1678
30	291	99	1690
50	255	88	1698
80	160	56	1699.2
120	39	24	1699.3
180	0.4	17	1699.3

FIG. 6. Melt undercooling and solid fraction as a function of droplet size.
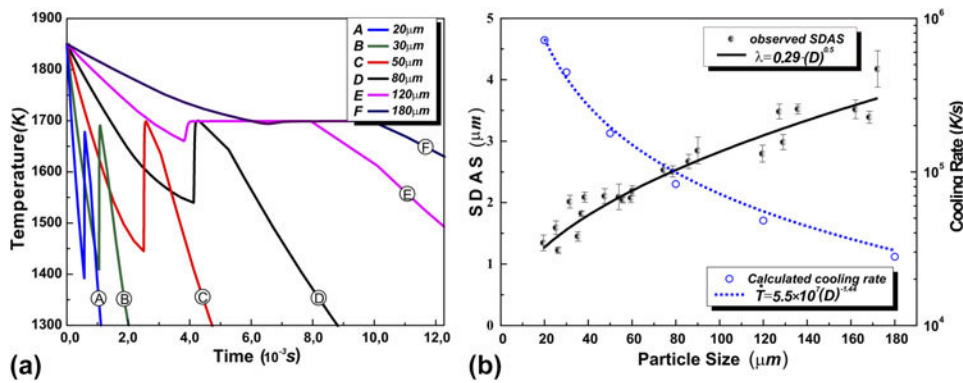
FIG. 7. (a) Cooling curves of different sized droplets and (b) SDAS and cooling of the droplets.

decreases to 20 μm, the undercooling (solid line in Fig. 6) reaches 302 K, very close to the reported maximum value of iron, 295 κ, reported by Turnbull.[31] Also, the solid fraction, as shown in dots, during recalescence is strongly affected by the prior undercooling of the droplet. Comparing to Al–4.5 wt% Cu alloy,[20] in the same 20 μm droplet, the solid fraction was reported to be around 23%, much smaller than that of Fe–6.5 wt% Si, and the reasons are attributed to the different physical properties of the alloys, such as latent heat of fusion, partition coefficient k, and the liquidus and solidus temperatures.

Referring to Fig. 4, the microstructure variation of the droplets is also strongly affected by the undercooling. In Fig. 4(c), the equiaxed dendritic morphology can be found in large particles. According to the work of Herlach,[32] the grain refined equiaxed microstructure, coming from the fragmentation of dendrites in the undercooled melt, is strongly related to the melt undercooling during solidification when the characteristic break-up time $\Delta t_{bu}(\Delta T)$ must be smaller than the plateau duration time $\Delta t_{pl}(\Delta T)$. The latter becomes shorter as the cooling rate grows larger, which is the case in smaller droplets. On the other hand, $\Delta t_{bu}(\Delta T)$ of certain undercooling is a constant. As a result, the higher cooling rate achieved in smaller droplets will lessen the chance of fragmentation as in larger droplets [Fig. 4(c)]. Also, as listed in Table I, the solid fraction at the end of recalescence f_r decreases from 99.2% in 20 μm to 17% in 180 μm, and the temperature T_r increases from 1678 to 1699 K, indicating the lower possibility of dendrite fragmentation in smaller droplets. This result is coincident with our observations that the fine-grained equiaxed structures are mostly found in large droplets.

The calculated cooling curves and the cooling rate are given as a function of the droplet size. As shown in Fig. 7(a), the cooling procedure of the droplet includes three parts: liquid state cooling, recalescence, and segregation solidification. The cooling rate in Fig. 7(b) here refers to the postrecalescence stage of solidification when the SDA is formed. The cooling rate of the droplet
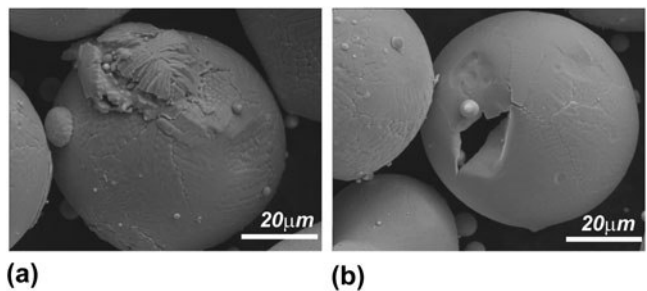

(a) (b)

FIG. 8. (a) The microstructure of the normal solidified droplet compared with (a) a broken piece and (b) a hollow shell to show the coarsening effect.

at postrecalescence state is very high, ranging from 10^4 to 10^6 K/s in magnitude.

The postrecalescence cooling rate of the droplet can be estimated by combining the observed SDAS as a function of the droplet size, $\lambda = 0.29 \cdot D^{0.5}$. Then, one can readily obtain the relationship between SDAS and cooling rate, $\lambda = 74.2 \cdot (\dot{T})^{-0.347}$. The relationship of the SDAS as a function of cooling rate is obtained in gas-atomized iron-based stainless steel,[33] $\lambda = 49.3 \cdot (\dot{T})^{-0.3}$ and Cu–Sn,[9] $\lambda = 37.31 \cdot (\dot{T})^{-0.338}$, indicating that the result of this work lies within the typical range of the gas atomization process.

After the initiation of the dendrites, the ripening effect became significant to influence the microstructure of the droplet as evidenced in Fig. 8. When a droplet is broken up by collision during solidification, the coarsening ended by the separation of dendrites and interdendritic liquids, as shown in Fig. 8(a), the SDA of broken part is therefore thinner than that of a fully solidified droplet below. The same thing happened for the hollow droplet shown in Fig. 8(b). The melt jetted out from a crack of solidified shell, and one can see the very fine dendrite pattern comparing to the full droplet beside. Therefore, to describe the microstructure evolution of the droplet, the coarsening effect must be taken into account here.

The plot of local solidification time versus droplet size is presented in Fig. 9(a) and its effect on the SDAS is also shown in Fig. 9(b), using the power law fitted
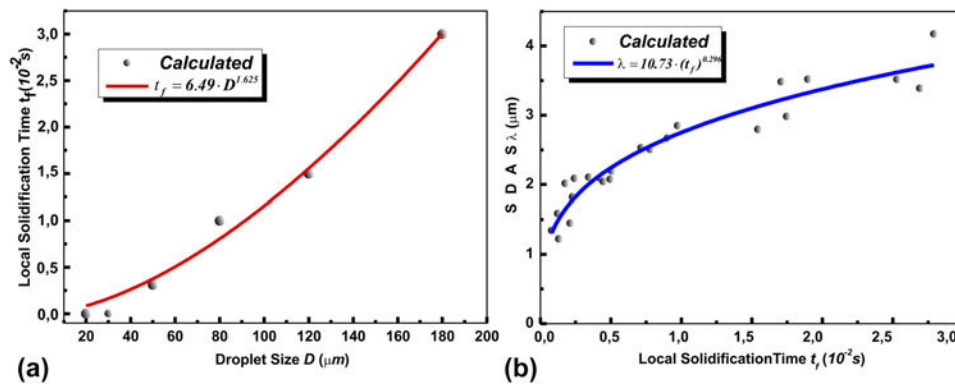
FIG. 9. (a) The calculated and fitted local solidification times for different droplet sizes and (b) the SDAS as a function of local solidification time.

relationship for droplets size and local solidification time. The SDAS varies with nearly the cubic root of local solidification time, which agrees quite well with the dendrite coarsening mechanism,[34,35] in which the SDAS is proportional to $t_f^{1/3}$.

VI. CONCLUSION

The Fe–6.5 wt% Si gas-atomized particles were fabricated and characterized, and the microstructure morphology of the particle is characterized by the SDAS as a function of droplet size, $\lambda = 0.29 \cdot D^{0.5}$. By applying the numerical model, the microstructure is further related to the solidification process of the droplet.

(1) The undercooling achieved prior to solidification can be very large and greatly influences the solid fraction at the end of recalescence.

(2) The cooling rate at the postrecalescence stage plays a critical role in the formation of SDA and is also very important for the "plateau" duration time, which decides the formation of the equiaxed dendritic morphology. The calculated result of the SDAS as a function of cooling rate $\lambda = 74.2 \cdot \left(\dot{T} \right)^{-0.347}$ compares fairly well to other gas-atomized alloys.

(3) The development of the SDA is characterized as a coarsening growth by relating the SDAS to the cubic root of local solidification time, $\lambda = 10.73 \cdot \left(t_f \right)^{0.296}$.

ACKNOWLEDGMENT

REFERENCES

1. K.I. Arai and K. Ishiyama: Recent developments of new soft magnetic materials. *J. Magn. Magn. Mater.* **133**(1–3), 233 (1994).
2. Y. Takada, M. Abe, S. Masuda, and J. Inagaki: Commercial scale production of Fe-6.5 wt. % Si sheet and its magnetic properties. *J. Appl. Phys.* **64**(10), 5367 (1988).
3. T. Yamaji, M. Abe, Y. Takada, K. Okada, and T. Hiratani: Magnetic properties and workability of 6.5% silicon steel sheet manufactured in continuous CVD siliconizing line. *J. Magn. Magn. Mater.* **133**(1–3), 187 (1994).
4. K.I.A.N. Tsuya: Ribbon-form silicon-iron alloy containing around 6.5 percent silicon. *IEEE Trans. Mag.* **16**(1), 4 (1980).
5. A.H. Kasama, A.J.J. Moreira, F°.W.J. Botta, C.S. Kiminami, and C. Bolfarini: Influence of the atomization gas on the microstructure and magnetic properties of spray-formed Fe–3%Si–3.5%Al alloys. *Mater. Sci. Eng., A* **477**(1–2), 9 (2008).
6. H. Shokrollahi and K. Janghorban: Soft magnetic composite materials (SMCs). *J. Mater. Process. Technol.* **189**(1–3), 1 (2007).
7. G.A.V. Sowter: Soft magnetic materials for audio transformers: History, production, and applications. *J. Audio Eng. Soc.* **35**, 760 (1987).
8. E. Bayraml, Ö. Gölgelioğlu, and H.B. Ertan: Powder metal development for electrical motor applications. *J. Mater. Process. Technol.* **161**(1–2), 83 (2005).
9. N. Tiedje, P.N. Hansen, and A.S. Pedersen: Modeling of primary and secondary dendrites in a Cu-6 wt pct Sn alloy *Metall. Mater. Trans. A* **27**(12), 4085 (1996).
10. A. Freyberg, M. Buchholz, V. Uhlenwinkel, and H. Henein: Droplet solidification and gas-droplet thermal coupling in the atomization of a Cu-6Sn alloy. *Metall. Mater. Trans. B* **34**(2), 243 (2003).
11. C.G. Levi and R. Mehrabian: Microstructures of rapidly solidified aluminum alloy submicron powders. *Metall. Mater. Trans. A* **13**(1), 13 (1982).
12. W.J. Boettinger, L. Bendersky, and J.G. Early: An analysis of the microstructure of rapidly solidified Al-8 wt pct Fe powder. *Metall. Trans. A* **17**(5), 781 (1986).
13. R. Xu, Y.Y. Cui, D. Li, D.M. Xu, Q.C. Li, and Z.Q. Hu: Solidification microstructure of super-α2 alloy prepared by gas atomization. *J. Mater. Sci.* **32**(14), 3821 (1997).
14. B. Zheng, Y. Lin, Y. Zhou, and E. Lavernia: Gas atomization of amorphous aluminum powder: Part II. Experimental investigation. *Metall. Mater. Trans. B* **40**(6), 995 (2009).
15. S. Li, P. Wu, H. Fukuda, and T. Ando: Simulation of the solidification of gas-atomized Sn-5mass%Pb droplets. *Mater. Sci. Eng., A* **499**(1–2), 396 (2009).

16. C.G. Levi and R. Mehrabian: Heat-flow during rapid solidification of undercooled metal droplets. *Metall. Trans. A* **13**(2), 221 (1982).

17. E.J. Lavernia, E.M. Gutierrez, J. Szekely, and N.J. Grant: A mathematical model of the liquid dynamic compaction process. Part 1: Heat flow in gas atomization. *Int. J. Rapid Solidification* **4**, 89 (1988).

18. E. Gutierrez-Miravete, E.J. Lavernia, G.M. Trapaga, J. Szekely, and N.J. Grant: A mathematical model of the spray deposition process. *Metall. Trans. A* **20**(1), 71 (1989).

19. P. Mathur, D. Apelian, and A. Lawley: Analysis of the spray deposition process. *Acta Metall.* **37**(2), 429 (1989).

20. E-S. Lee and S. Ahn: Solidification progress and heat transfer analysis of gas-atomized alloy droplets during spray forming. *Acta Metall. Mater.* **42**(9), 3231 (1994).

21. D. Bergmann, U. Fritsching, and K. Bauckhage: A mathematical model for cooling and rapid solidification of molten metal droplets. *Int. J. Therm. Sci.* **39**(1), 53 (2000).

22. N.H. Pryds and J.H. Hattel: Spray forming: A numerical investigation of the influence of the gas to melt ratio on the billet surface temperature. *Int. J. Therm. Sci.* **44**(6), 587 (2005).

23. R. Heringer, C.A. Gandin, G. Lesoult, and H. Henein: Atomized droplet solidification as an equiaxed growth model. *Acta Mater.* **54**(17), 4427 (2006).

24. N. Zeoli, S. Gu, and S. Kamnis: Numerical modelling of metal droplet cooling and solidification. *Int. J. Heat Mass Transfer* **51**(15–16), 4121 (2008).

25. B. Zheng, Y. Lin, Y. Zhou, and E. Lavernia: Gas atomization of amorphous aluminum: Part I. Thermal behavior calculations. *Metall. Mater. Trans. B* **40**(5), 768 (2009).

26. H. Okamoto: *Phase Diagrams for Binary Alloys*, 2nd ed. (ASM International, 2000).

27. R. Trivedi and K. Somboonsuk: Constrained dendritic growth and spacing. *Mater. Sci. Eng.* **65**(1), 65 (1984).

28. J.P. Hirth: Nucleation, undercooling and homogeneous structures in rapidly solidified powders. *Metall. Trans. A* **9**(3), 401 (1978).

29. W. Kurz and D.J. Fisher: *Fundamentals of Solidification*, 4th ed. (Trans. Tech. Publications, 1998).

30. K-C. Chang and C-M. Chen: Revisiting heat transfer analysis for rapid solidification of metal droplets. *Int. J. Heat Mass Transfer* **44**(8), 1573 (2001).

31. D. Turnbull and R.E. Cech: Microscopic observation of the solidification of small metal droplets. *J. Appl. Phys.* **21**(8), 804 (1950).

32. D.M. Herlach, K. Eckler, A. Karma, and M. Schwarz: Grain refinement through fragmentation of dendrites in undercooled melts. *Mater. Sci. Eng., A* **304–306**(0), 20 (2001).

33. N.H. Pryds and A.S. Pedersen: Rapid solidification of martensitic stainless steel atomized droplets. *Metall. Mater. Trans. A* **33**(12), 3755 (2002).

34. T.Z. Kattamis and M.C. Flemings: Dendrite morphology, microsegregation, and homogenization of low-alloy steel. *Trans. Metall. Soc. AIME* **223**, 8 (1965).

35. S.P. Marsh and M.E. Glicksman: Overview of geometric effects on coarsening of mushy zones. *Metall. Mater. Trans. A* **27**(3), 557 (1996).